International Journal of Impact Engineering 152 (2021) 103825

Contents lists available at ScienceDirect

International Journal of Impact Engineering

journal homepage: www.elsevier.com/locate/ijimpeng

Finite element analysis of porous polymer coated pipelines subjected to impact

Ole Vestrum [a,b,*], Magnus Langseth [a,b], Tore Børvik [a,b]

[a] Structural Impact Laboratory (SIMLab), Department of Structural Engineering, NTNU – Norwegian University of Science and Technology, Trondheim, Norway
[b] Centre for Advanced Structural Analysis (CASA), NTNU, Trondheim, Norway

ARTICLE INFO

Keywords:
Porous coating
Pipelines impact
Indentation tests
FE simulation
X-ray CT
Thermal softening,

ABSTRACT

Subsea steel pipelines are often coated with external polymer coatings. While primarily applied for corrosion protection and thermal insulation, such coatings have been shown to contribute significantly to the energy absorption during impact events. However, due to the lack of reliable models accounting for the complex coating features, positive contributions from the coating to the mechanical response of the pipeline are often omitted in design. In a previous study, samples of a typical polymer coating were scanned using X-ray micro computed tomography (XRMCT) and the density mappings were applied to build finite element (FE) models of the porous morphology. These FE models were then used to calibrate a constitutive material model, which takes the porosity of the coating into account. It was concluded that the constitutive model may be applied in large-scale FE simulations of coated pipelines. In this work, the calibrated constitutive model is used to simulate the response of quasi-static indentation and impact tests performed on full-scale offshore pipeline components with and without multi-layered polymeric coating. The objectives of the work are to evaluate the performance of the originally presented model and to implement modifications essential in capturing the physical phenomena of the problem. The original model is seen to describe the early parts of the deformation very well. However, some deviations are seen as the coating becomes severely compressed between the indenter and the steel pipe. A strain- and porosity-based fracture criterion is therefore implemented, which alleviates the problem and produces a good correspondence between simulations and experiments. Modifications are also made to the coating model to include dependencies of strain-rate and temperature in the coating material response. The modified model is calibrated to strain-rate and temperature data retrieved from a similar polymer material found in the literature. Case studies with simulations of impact events under various strain-rate and temperature conditions are performed. The simulation results are compared to quasi-static indentation and impact tests presented in previous works. These results give indications that the strain-rate and thermal sensitivity of the coating material should be further explored.

1. Introduction

The offshore petroleum industry uses vast networks of pipelines to convey crude oil and natural gas along the ocean floor. These pipelines are in certain cases left exposed and vulnerable when dedicated protective measures (e.g., burial, trenching, armored coatings or protective covers) are impracticable or too expensive [1,2]. However, the pipelines are often externally covered with coating solutions serving other primary purposes than physical protection – such as anti-corrosion, anti--buoyancy or thermal insulation. While not primarily indented for it, these coating solutions are experienced to influence the structural integrity of the pipelines [3–5], like in the event of impact from moving objects [6]. Subsea installations tend to attract fish [2], which contributes to increased fishing activities in these areas and increased risk of impact from fish trawling equipment [2,6] or falling anchors [3,7]. Interaction events between pipelines and moving objects have been studied extensively in the literature [8–13]. Although various coating solutions are experienced to influence the pipeline integrity [3,4,14], the coatings' positive contributions are often omitted during the design process due to their complex features. Vestrum et al. [15] conducted a series of quasi-static indentation and impact tests on full cross-sectional 1 meter long pipeline specimens coated with a thermal insulation

* Corresponding author.
E-mail address: ole.vestrum@ntnu.no (O. Vestrum).

https://doi.org/10.1016/j.ijimpeng.2021.103825
Received 16 September 2020; Received in revised form 26 December 2020; Accepted 25 January 2021
Available online 30 January 2021

coating product with two different design configurations. The experiments were conducted on both coated and uncoated specimens, and a significant contribution to the total energy absorption during impact provided by the coatings themselves was proven. In subsequent work by some of the same authors [16], X-ray micro computed tomography (XRMCT) was used to derive multi-scale models of cylindrical samples of the porous material, which isolated the contributions made on the various scales to the total mechanical behavior of the coating. Therein, it was found that the response was governed by a combination of the behavior of the constituent polymeric material (microscopic scale) and the insulating porous structure (macroscopic scale). Variations in key features were documented through the coating thickness on both scales. Following this, Vestrum et al. [17] derived a constitutive model for the mechanical behavior of the coating by mapping the pressure sensitivity of the porous coating's yield strength at smaller discrete regions through the thickness of the coating based on unit cell simulations. The calibrated constitutive model is a mere function of the macroscopic porosity, which evolves with deformation.

The objective of this work is to investigate the performance of the constitutive model made for the porous polymer pipeline coating presented by Vestrum et al. [17] in estimating the mechanical response of coated pipelines subjected to impact events. The experimental results from quasi-static indentation and impact tests on two different pipe cross-sectional designs conducted by Vestrum et al. [15] are used as the basis for evaluating the framework. During this work, some discrepancies between the experimental results and the numerical simulations using the original coating model presented in [17] become apparent. Modifications are therefore made to the constitutive coating model to study the influence of strain-rate and temperature sensitivity in the solid phase polymer to the global response of the component during different loading events. As the characterization of the said phenomena in the polymer material applied herein is too extensive, such studies are omitted in this work. Instead, test data for a polymer similar to the coating material applied in this study are retrieved from the literature and used to calibrate the modified material description. This calibration merely serves as a means in evaluating how the strain rate and temperature may influence the global pipeline response, and not as an accurate representation of the coating material's sensitivity to the said material effects. A set of case studies is also presented where the behavior of the modified model is studied under different conditions. One of these case studies is an uncoupled thermal-mechanical evaluation of the modified model. To this end, the thermal conductivity across the porous coating is numerically estimated using models of the coatings' pore morphology collected with XRMCT. The estimated thermal conductivity is used with a realistic temperature scenario for pipelines in operation to produce corresponding temperature fields that vary through the components. These temperature fields are used with the modified coating model to investigate the potential consequence temperature gradients may have on the global response of pipelines during impact events. Finally, the results are evaluated, conclusions are reached and some suggestions for further efforts are made.

2. Materials and methods

2.1. Pipeline designs

Pipeline components pertaining to two different cross-sectional designs (denoted Pipe S and Pipe L) have been studied in the work. Various aspects of these designs have previously been investigated experimentally [15,16] and numerically [16,17]. Both designs consist of an inner X65 steel pipe externally covered with a multi-layer polypropylene coating solution, but the designs differ in terms of dimensions and layer composition. Fig. 1 shows quartile cross-sectional views of both Pipe S and Pipe L with applied dimensions.

The mechanical behavior of the X65 steel pipe has previously been studied in depth by Kristoffersen et al. [18], 19]. Vestrum et al. [15] also

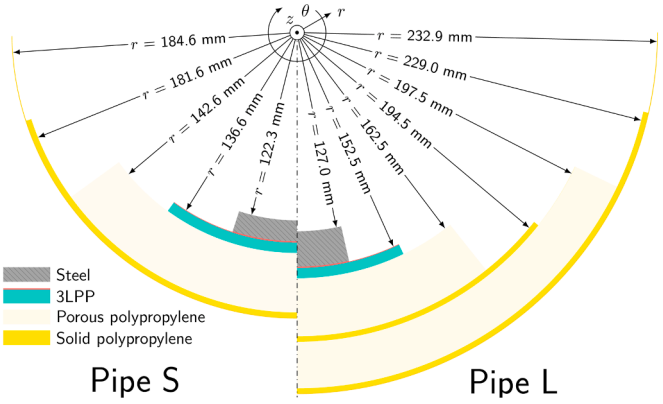

Fig. 1. Quartile cross-sectional view (w/ dimensions) of the layer composition of Pipe S and Pipe L.

conducted a series of tensile tests on the X65 steel material of both Pipe S and Pipe L. The work presented herein employs this material data for the X65 steel to calibrate the material behavior of the component simulations presented in the following. The axisymmetric tensile specimens were sampled from the same component specimens as tested in the quasi-static indentation and impact experiments. To utilize the experimental data in the numerical simulations in this study, the elastic-plastic behavior must be formalized. A two-term Voce constitutive relation was used to model the strain hardening, viz.

$$\sigma = \sigma_0^{X65} + \sum_{i=1}^{2} Q_i \left(1 - \exp(-\beta_i p)\right) \tag{1}$$

where σ_0^{X65} is the initial yield strength, p is the equivalent plastic strain and (Q_i, β_i) are hardening parameters. The model parameters were calibrated to the X65 steel tensile tests' true stress-strain data using the method of least squares, which are given in Table 1 along with the elastic parameters used herein.

The multi-layer coating solution is the main modeling focus of this work. The solution is known under the product name Thermotite (polypropylene foam) and produced by Shawcor [20]. The general coating solution consists of different layers of polypropylene serving various primary purposes. A 3-layer polypropylene (3LPP) coating is applied to provide adhesion and to protect the steel pipe from corrosion. A layer-set of porous and solid polypropylene is subsequently applied on the outside of the 3LPP. The porous layer provides significant thermal insulation while the solid layer provides a shield against the harsh ambient seawater environment. Pipe S has one such layer-set of porous and solid polypropylene, while Pipe L has two for improved thermal insulation. In this work, the multi-layer coatings will be studied and modeled as a single continuous component with varying macroscopic pore morphology. Previous work [16,17] has revealed a complex variation in both micro- and macroscopic material properties across the coating thickness, which affects the mechanical behavior. Vestrum et al. [17] presented techniques for modeling the mechanical behavior of the coating material through evaluations of the porosity. These modeling techniques are utilized in this work to model the coating.

Table 1
Calibrated material model parameters for X65 steel based on data from Vestrum et al. [15].

Elastic		Plastic				
E	ν	σ_0^{X65}	Q_1	β_1	Q_2	β_2
[GPa]	[]	[MPa]	[MPa]	[ ]	[MPa]	[ ]
208	0.3	488.9	122.3	30.1	2151.4	0.2

2.2. Strain-rate and temperature sensitivity of polypropylene

The mechanical behavior of polymer materials is known to be sensitive to variations in both strain rate and temperature [21]. The contribution made by the polymer in the original coating model presented in [17] is invariant of either effect. To investigate how differences in strain rate and temperature may influence the full-scale response, a modified coating model will be introduced in Section 3. However, a calibration of this model requires experimental data of the polymer material's behavior under various strain-rate and temperature conditions. As this requires significant efforts such experimental studies are excluded in order to sharpen the focus of this work. Instead, a literature source is used to provide the necessary material data. Johnsen et al. [21] performed an extensive study into the influence of strain rate and temperature on the yield strength of a similar polypropylene material used in pipeline coatings made by the same producer as the coating material studied herein. The data generated in that study is summarized in Table 2.

The mechanical contribution made by the polymer material was modeled with a perfect plastic representation using a yield strength of 28 MPa. This value was obtained under approximate quasi-static (i.e. $\dot{p} = 0.001\ s^{-1}$) and room temperature conditions (i.e. $T = 296.15$ K) in previous work [16,17]. Thus, it is necessary for the calibrated model to produce a yield strength of 28 MPa under quasi-static and room temperature conditions. When studying the values in Table 2, it becomes obvious that a direct calibration of a strain-rate and temperature dependent yield strength relation with this data set will produce a yield strength value that is lower than that of 28 MPa under the said conditions. To this end, it is necessary to scale to values of Table 2 to ensure that the calibrated model produces the sought response under quasi-static and room temperature condition. This scaling will be presented under Section 4.1.

2.3. Full-scale pipeline experiments

As previously stated, Vestrum et al. [15] presented a series of quasi-static indentation and impact tests conducted on 1 meter long pipeline samples of Pipe S and Pipe L. The study demonstrated the significant mitigating effect, in terms of energy absorption, provided by the coating during impact events. These experiments provide realistic validation cases for the constitutive coating model. While the loading-rate differed, the quasi-static setup was considered equivalent to the dynamic in terms of boundary conditions. Thus, a single setup is modeled in the simulations, but the loads are applied differently. Fig. 2 presents sketches of the setup used for both the quasi-static indentation and impact simulations. While a detailed presentation is given in [15], some essential details related to the experimental work are outlined below:

- The quasi-static indentation experiments were performed under displacement control in a general-purpose test machine where the indenter was displaced into the pipeline specimens utilizing a hydraulic piston. These tests were performed under sequential loading-unloading, which may be seen in the force-displacement data plotted in Section 5.3.
- A testing facility known as the kicking machine [22] was used to perform the impact experiments. There, a trolley of mass $m = 1472$ kg with the same indenter as used in the quasi-static tests mounted to it was accelerated to velocities corresponding to a sought kinetic energy. The trolley was guided by a set of rails at which the pipeline specimens were placed at the end. A load cell measured the reaction forces and a high-speed camera recorded images from the impact region during the tests.
- The indenter design applied in the experiments had the sharpest nose profile outlined by the utilized guideline [2]. A detailed drawing of the indenter is given by Vestrum et al. [15]. This contributed to the rupturing of the polymer layers as the coating was compressed by the indenter. This is depicted in Fig. 3, which shows the aftermath of the quasi-static indentation of a Pipe L specimen. A distinct fracture zone running down to the steel pipe is seen.
- The outer deformation at the tip of the indenter nose is denoted u_o, the deformation of the inner steel pipe is denoted u_i and the reaction force (parallel to the moving direction of the indenter) experienced by the indenter is denoted F. These values were continuously measured in all tests.

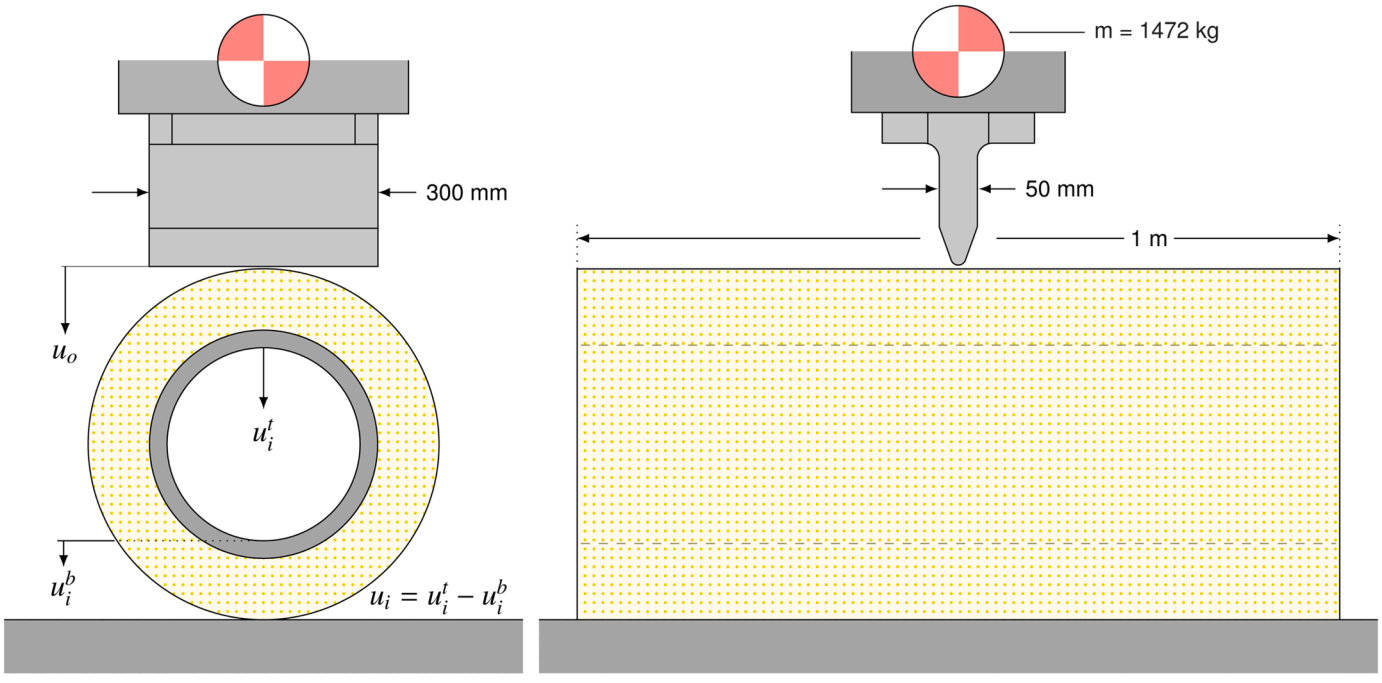

Fig. 2. Fundamental setup applicable for both the quasi-static indentation and the dynamic impact experiments.

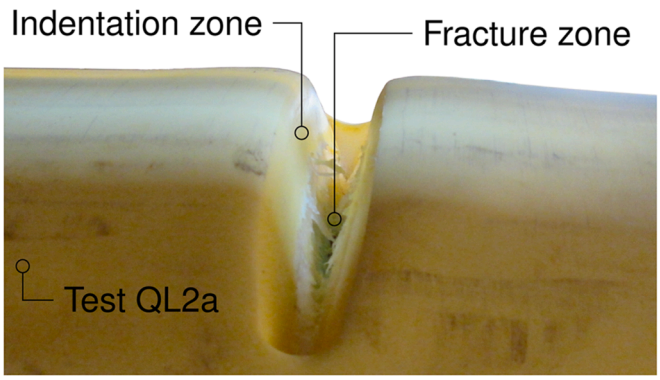

Fig. 3. Fracture in coating under quasi-static indentation.

Table 3 lists the tests from [15] which were simulated in this study. The force-deformation data collected from these tests were use in evaluating the accuracy of the simulations. These results will be presented alongside the numerical results under Section 5.

2.4. X-ray micro computed tomography

The constitutive coating model (see Section 3) relies on the macroscopic porosity of the coating material as input. While the porosity of the coating material of Pipe S has been mapped in previous work [15–17], Pipe L's coating remains to be studied. Therefore, an XRMCT scan is performed on a coating specimen from Pipe L. Fig. 4(a) presents the coating specimens and Fig. 4(b) shows the respective specimen placed in the XRMCT setup. The same acquisition and post-processing procedures as in [17] were conducted on the specimen herein. Fig. 4(c) presents a gray-scale image slice of the reconstructed XRMCT data. The XRMCT data is exported as a 3D matrix with integer entries (i.e. voxels) given on an 8-bit gray-scale (i.e. a value between 0 and 255) related to the local density of each voxel. This data is referred to as a voxel matrix in [17] – a term that is also adopted in this work.

Vestrum et al. [16] presented a post-processing procedure for converting the voxel matrices into FE models. Since the voxel matrices of both Pipe S and Pipe L are to be used in the thermal studies presented Section 5.5.2, a summary of the procedure is provided herein. The procedure applies a series of processing steps to the raw voxel matrix, which is illustrated in Fig. 5. As the XRMCT technique is sensitive to noise, the raw voxel matrix (Fig. 5(a)) is filtered using a bilateral filter [23] to produce a filtered voxel matrix (Fig. 5(b)). The filtered voxel matrix contains too much information (the original voxel side length resolutions of the matrix of Pipe S and Pipe L were 0.035 mm and 0.048 mm, respectively) for being efficiently processed by subsequent steps and the resolution must be reduced (Fig. 5(c)). The final voxel side resolutions were 0.08 mm in this work. Finally, the reduced resolution voxel matrix is binarized with a threshold value established by Otsu's method [24]. The binary voxel matrix may then be converted into FE meshes readable by commercial finite element codes. For a detailed description of each step in the procedure, the reader is referred to the work by Vestrum et al. [16].

Table 2
Temperature, strain-rate and yield strength data for the polypropylene material [21] used as basis for the calibration of the modified coating model used herein.

	$\dot{p} = 0.01$	$\dot{p} = 0.1$	$\dot{p} = 1.0$	[s^{-1}]
T [K]	σ_0^*	σ_0^*	σ_0^*	[MPa]
298.15	19.10	20.90	22.86	
273.15	24.82	26.91	28.92	
258.15	28.84	31.15	34.80	
243.15	34.10	36.92	43.90	

Table 3
Overview of full-scale experiments by Vestrum et al. [15] that are used to compare with simulations.

ID	Coated	v_0 [m/s]	E_{kin} [kJ]
QS1	No	-	-
QS2	Yes	-	-
DS4a	Yes	3.70	10.1
QL1	No	-	-
QL2a	Yes	-	-
DL4a	Yes	3.77	10.5
DL2a	Yes	5.14	19.4

3. Constitutive coating model

3.1. Preliminary

The governing equations of the constitutive model applied to the coating material are presented in the following sections. The model was originally formulated, implemented, calibrated and validated by Vestrum et al. [17]. In this work, however, modifications are made to the original model. The modifications include strain-rate and temperature dependence in the yield strength response to investigate the influence of these phenomena on the global response. Additionally, a need for eroding excessively deformed coating elements was seen during preliminary simulations using the original implementation. To this end, a fracture criterion governing element erosion was added. While Section 3.2 and Section 3.3 presents the governing equations, which are also valid for the original model, Section 3.4 and Section 3.5 highlight the modifications made.

3.2. Formulation

A hypoelastic-plastic formulation was chosen for the coating material in this study. The rate-of-deformation tensor $\mathbf{D}$ is additively decomposed into an elastic part $\mathbf{D}^e$ and a plastic part $\mathbf{D}^p$ through the relation

$$\mathbf{D} = \mathbf{D}^e + \mathbf{D}^p \tag{2}$$

The elastic part is described by the generalized Hooke's law, viz.

$$\mathbf{D}^e = \frac{1+\nu}{E}\boldsymbol{\sigma}^{\nabla GN} - \frac{\nu}{E}\mathrm{tr}(\boldsymbol{\sigma}^{\nabla GN})\mathbf{I} \tag{3}$$

where $\boldsymbol{\sigma}^{\nabla GN}$ is the objective Green-Nagdhi rate of the Cauchy stress tensor, E is the elastic modulus, ν is the Poisson ratio and $\mathbf{I}$ is the second-order unit tensor. Vestrum et al. [16] found that $E_{pp} = 800$ MPa and $\nu_{pp} = 0.4$ for the constituent polypropylene material of the porous layer were good matches. As the elastic parameters of cellular materials are known to depend on porosity [25], linear scaling relations are assumed for E and ν so that

$$E = E(f) = (1-f)E_{pp} \quad \text{and} \quad \nu = \nu(f) = (1-f)\nu_{pp} \tag{4}$$

where f is the porosity of the porous solid. The porosity is a key parameter in also other parts of the constitutive description. The porosity f of the coating material is defined as

$$f = \frac{V_p}{V} \tag{5}$$

where V_p is the volume occupied by the pores and V is the total volume of the porous solid. Associated plastic flow is assumed, which defines the plastic rate-of-deformation tensor through

$$\mathbf{D}^p = \dot{\lambda}\frac{\partial \Phi}{\partial \boldsymbol{\sigma}} \tag{6}$$

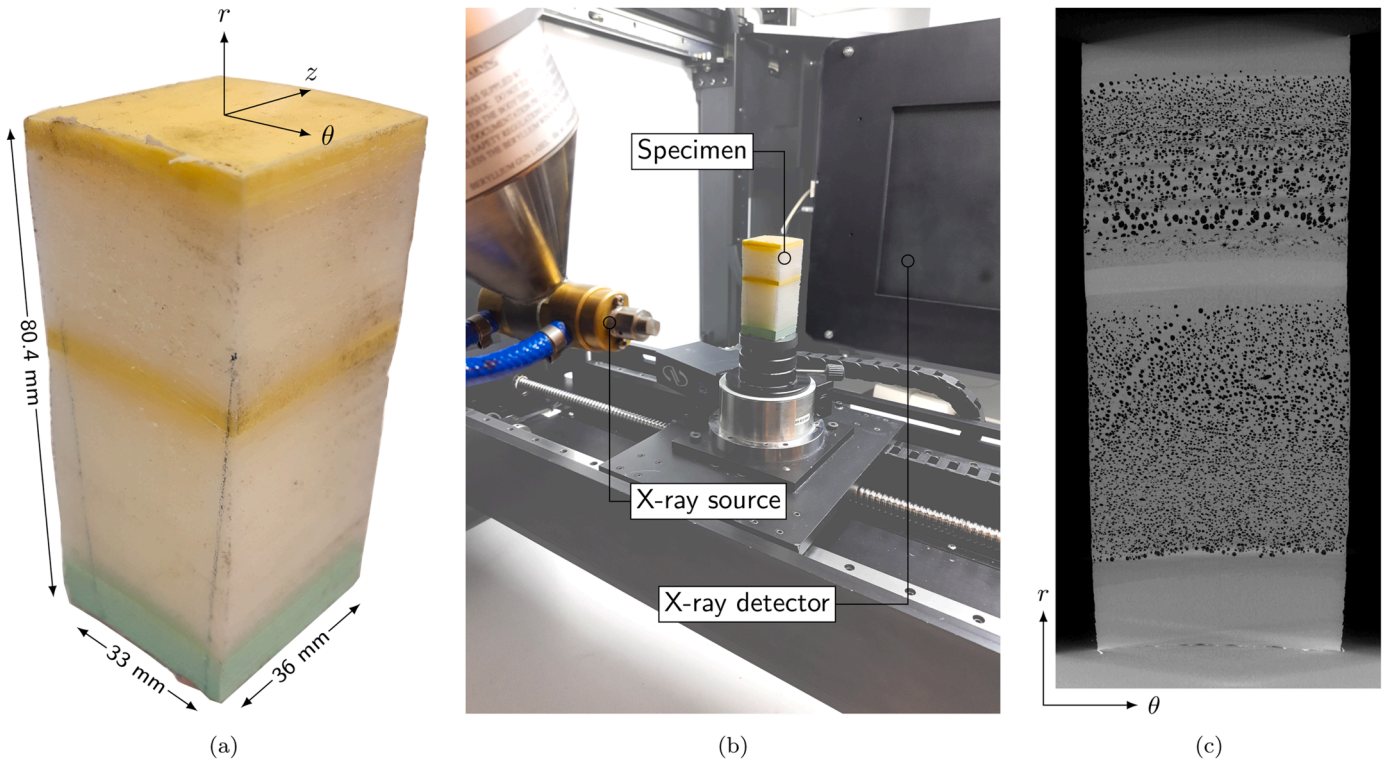

Fig. 4. (a) Pipe L specimen with approximate measurements placed inside the (b) XRMCT setup and (c) a gray-scale 2D image slice of the constructed XRMCT voxel data.

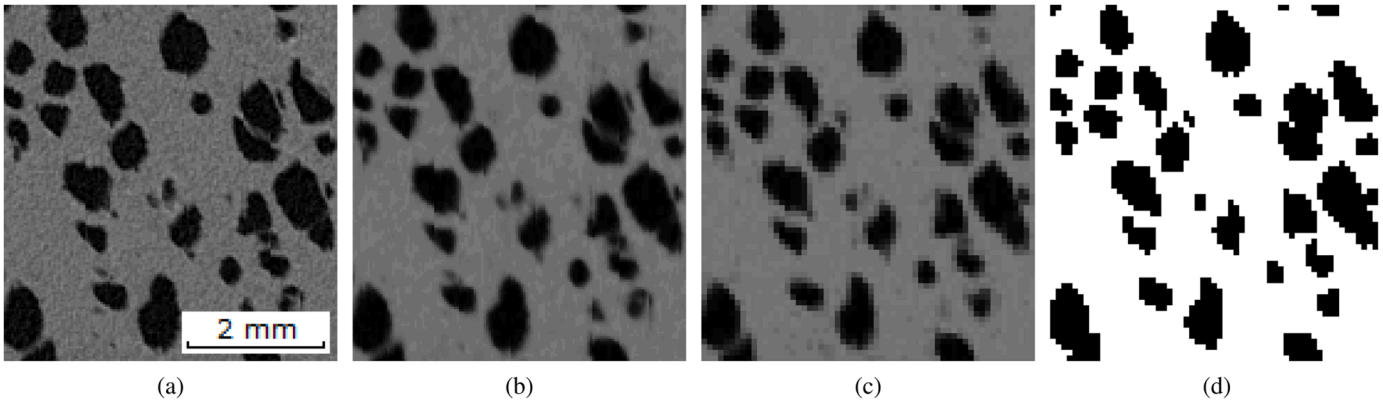

Fig. 5. Cross-section slices of (a) the voxel matrix (0.035 mm/px in image) with (b) filtering, (c) down-scaling (0.08 mm/px in image) and (d) binarization.

where $\dot{\lambda}$ is the plastic multiplier, Φ is the applied yield function and $\boldsymbol{\sigma}$ is the Cauchy stress tensor. The Deshpande-Fleck [26] yield function, which is a much used model for foamed materials, was employed, viz.

$$\Phi = \sigma_{\text{eq}}^{\text{DF}} - \sigma_y \tag{7}$$

where $\sigma_{\text{eq}}^{\text{DF}}$ is the Deshpande-Fleck equivalent stress measure given as

$$\sigma_{\text{eq}}^{\text{DF}} = \sqrt{\frac{1}{1+\left(\frac{\alpha}{3}\right)^2}\left[\left(\sigma_{\text{eq}}^{\text{VM}}\right)^2 + (\alpha\sigma_{\text{H}})^2\right]} \tag{8}$$

In Eq. 8, $\sigma_{\text{eq}}^{\text{VM}}$ and σ_{H} are the von Mises equivalent stress and the hydrostatic stress, respectively, given as

$$\sigma_{\text{eq}}^{\text{VM}}\left(\boldsymbol{\sigma}\right) = \sqrt{\frac{3}{2}\boldsymbol{\sigma}' : \boldsymbol{\sigma}'} \quad \text{and} \quad \sigma_{\text{H}}\left(\boldsymbol{\sigma}\right) = \frac{1}{3}\text{tr}(\boldsymbol{\sigma}) \tag{9}$$

Additionally, α and σ_y are model parameters governing the shape and size of the yield surface, respectively. Plasticity occurs under the condition $\Phi = 0$, a state which defines the yield surface. The loading-unloading conditions in Kuhn-Tucker form [27] are given as

$$\Phi \leq 0, \quad \dot{\lambda} \geq 0, \quad \dot{\lambda}\Phi = 0 \tag{10}$$

with the consistency condition given through

$$\dot{\lambda}\dot{\Phi} = 0 \tag{11}$$

By applying associated plastic flow and equivalence in plastic power (i.e. $\boldsymbol{\sigma}:\mathbf{D}^{\text{p}} = \sigma_y\dot{p}$) it may be shown that $\dot{p} = \dot{\lambda}$ where $\dot{p}$ is the rate of the equivalent plastic strain conjugate to the yield stress σ_y.

3.3. Evolution of porosity

As the various parameters in the model scale with the porosity, an

evolution law for f is defined, viz.

$$\dot{f} = (1-f)\mathrm{tr}(\mathbf{D}^{\mathrm{p}}) = (1-f)\dot{\lambda}\frac{\alpha^2\sigma_{\mathrm{H}}}{\sigma_{\mathrm{eq}}^{\mathrm{DF}}\left[1+\left(\frac{\alpha}{3}\right)^2\right]} \tag{12}$$

As no work hardening occurs in the constitutive model, it is important to note that any evolution of the yield surface during deformations (i.e. under static and isotherm conditions for the modified implementation) is caused by the evolution of f.

3.4. Strain-rate and temperature dependence

As mentioned in Section 3.3, the evolution of the yield surface in the initial model is a mere function of f. It is necessary to relate variables governing the plasticity behavior to the porosity of the porous solid in order to ensure a continuous evolution of the model behavior. Vestrum et al. [17] modeled the governing shape parameter α of the yield surface as

$$\alpha(f) = B_1 f^{B_2} \tag{13}$$

while the size parameter σ_y was defined as

$$\sigma_y(f) = \sigma_0 \exp(C_1 f). \tag{14}$$

where σ_0, B_1, B_2 and C_1 are model constants, which need to be calibrated. In the modified model, alterations were made to the governing equations in order to include strain-rate and temperature effects. A modified version [28,29] of the well-known Johnson-Cook [30] constitutive relation was employed to model the mentioned dependencies by making the constant σ_0 (in Eq. 14) a function of the equivalent plastic strain rate $\dot{p}$ and the temperature T, so that

$$\sigma_0 = \sigma_0\left(\dot{p}, T\right) = \widetilde{\sigma}_0\left[1+\frac{\dot{p}}{\widetilde{\dot{p}}}\right]^c\left[1-(T^*)^m\right] \tag{15}$$

where

$$T^* = \frac{T-\widetilde{T}}{T_m-\widetilde{T}} \tag{16}$$

In Eq. 15, the constants $\widetilde{\sigma}_0$, $\widetilde{\dot{p}}$ and $\widetilde{T}$ correspond to the yield stress, strain rate and temperature at a reference state, respectively, T_m is the melting temperature of the material, while c and m are material constants controlling the strain-rate sensitivity and thermal softening, respectively. Inserting Eq. 15 in Eq. 14, an updated expression for the yield strength σ_y of the coating material may be formulated as

$$\sigma_y(f, \dot{p}, T) = \sigma_0\left(\dot{p}, T\right)\exp(C_1 f) \tag{17}$$

A material user subroutine for the coating model was implemented in Abaqus/Explicit by Vestrum et al. [17]. Therein, the porosity update was made explicit meaning that the porosity was kept constant during return-mapping iterations. In order to ensure the numerical stability of the constitutive model with the modifications applied, the return-mapping was altered to include interactive updates of the porosity and strain rate. Because of this, the expression for α had to be changed to ensure that $\partial\alpha/\partial f$ did not evaluate to zero for $f = 0$. The updated expression fitted to the numerical yield loci data from [17] reads

$$\alpha(f) = B_1(1-\exp(B_2 f)) \tag{18}$$

in the modified model where B_1 and B_2 are parameters to be calibrated.

3.5. Fracture criterion

As the coating was seen to rupture during testing, a strain- and porosity-based fracture criterion was added to the model implementation. Note that the intention of including a fracture criterion is to alleviate numerical problems that arose due to excessive element distortion in preliminary analyses. Abaqus/Explicit allows for elements to be eroded when a given condition defined in the subroutine is violated. To this end, a damage variable Ψ was defined such that when

$$\Psi \geq \Psi_{\mathrm{critical}} \tag{19}$$

the respective element is eroded. Ψ is defined as an equivalent plastic strain accumulated only when the coating is below a certain porosity. This may be formulated as

$$\Psi_{t+\Delta t} = \Psi_t + \Delta p \quad \text{if} \quad f < f_{\mathrm{limit}} \quad \text{else} \quad \Psi_{t+\Delta t} = \Psi_t \tag{20}$$

where t is the time at the previous time step, $t+\Delta t$ is the time of the current time step and f_{limit} is a porosity limit value for when the coating is considered dense enough to accumulate damage (i.e. no damage accumulation occurs at larger porosities). Ψ_{critical} is a threshold value, which must be given as an input to the constitutive coating models. It is stated that this threshold value is sensitive to the applied mesh, and should therefore be used with care.

4. Calibration of the constitutive model

4.1. Strain-rate and temperature dependence

The calibration of the strain-rate and temperature terms in the modified model to the material data presented in Section 2.2 is given in this section. As argued in the mentioned section, a scaling of the data set presented in Table 2 was necessary in order to make the modified model comparable to the original implementation under quasi-static and room temperature conditions (i.e. $T = 296.15$ K and $\dot{p} = 0.001$ s^{-1}). The foundation of this scaling are given below. First, a intermediate calibration of c and m in Eq. 15 to the data in Table 2 was conducted using multi-dimensional curve-fitting in Python. This produced an expression for σ_0^* as a continuous function of $\dot{p}$ and T. The astrix (*) notation is used to denote *unscaled* values for the yield strength. The calibration was used to estimate the quasi-static response at room temperature for the polypropylene material investigated by Johnsen et al. [21], viz.

$$\sigma_0^*\left(\dot{p} = 0.001\ \mathrm{s}^{-1}, T = 296.15\ \mathrm{K}\right) = 19.05\ \mathrm{MPa} \tag{21}$$

This yield strength value is lower than the response of the polypropylene material studied in this work under comparable conditions (i.e. 28 MPa). Thus, a scaling of the data found in Table 2 was necessary to ensure that Eq. 15 will evaluate to 28 MPa under $\dot{p} = 0.001$ s^{-1} and $T = 296.15$ K when finally calibrated. Continuing, the yield strength values found in Table 2 was scaled according to the linear relation

$$\sigma_0 = \omega\ \sigma_0^* \tag{22}$$

where

$$\omega = \frac{28.0\ \mathrm{MPa}}{\sigma_0^*(\dot{p} = 0.001\ \mathrm{s}^{-1}, T = 296.15\ \mathrm{K})} = \frac{28.0}{19.05} = 1.47 \tag{23}$$

before the final calibration of c and m in Eq 15 was performed. The full set of calibrated parameter values used with Eq. 15 is provided in Table 4. Fig. 6 presents the mechanical response for the polypropylene material using the calibrated modified Johnson-Cook relation. Fig. 6(a) plots both the unscaled (unfilled markers) and scaled (filled markers) yield strength values versus strain rate, including graphs produced using

Table 4
Parameter values of Eq. 15 used in the modified coating model.

$\widetilde{\sigma}_0$ [MPa]	$\widetilde{\dot{p}}$ [s^{-1}]	$\widetilde{T}$ [K]	T_m [K]	c [ ]	m [ ]
49.9	0.01	243.14	436.15	0.0499	0.632

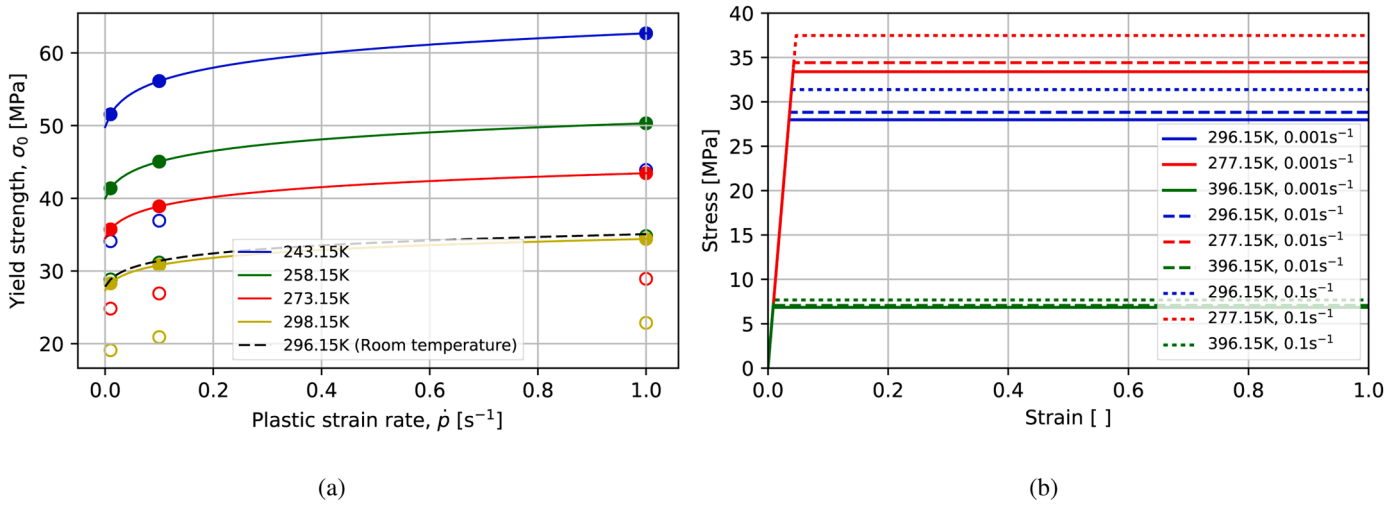

(a) (b)

Fig. 6. Response produced using the calibrated modified Johnson-Cook relation in terms of (a) yield strength-strain rate at various temperatures and (b) the elastoplastic stress-strain response under different conditions. The unfilled markers in (a) are the unscaled experimental yield strength values from Table 2, while the corresponding filled markers are the scaled values.

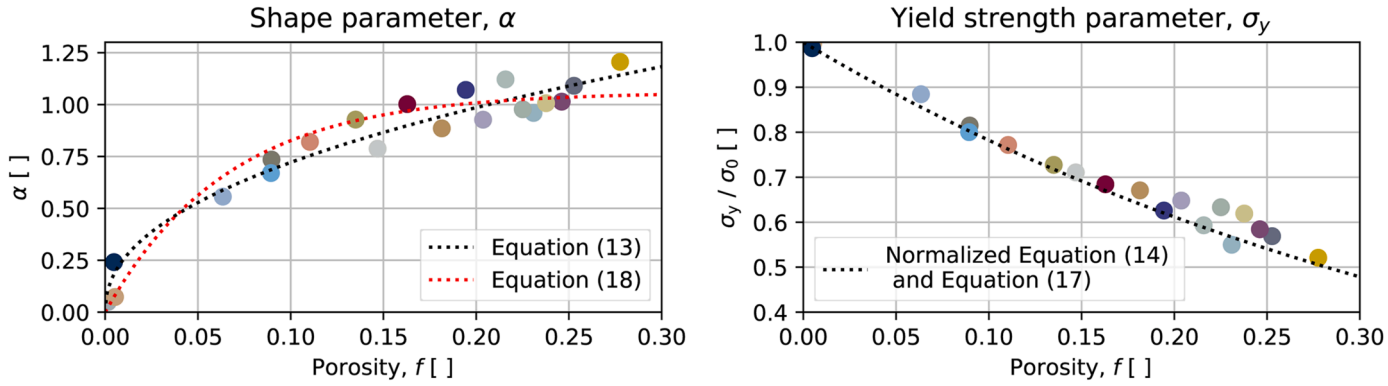

(a) (b)

Fig. 7. Scatter data produced by Vestrum et al. [17] with fittings of the parameter expressions for (a) α and (b) σ_y normalized with σ_0 for both model versions.

the calibrated modified Johnson-Cook relation, at different temperatures. Fig. 6(b) shows the full elastoplastic stress-strain response for the polypropylene material under a selection of strain-rate and temperature combinations.

4.2. Porosity dependence

Vestrum et al. [17] performed limit analyses on unit cell models derived from sublayers of a voxel matrix produced by XRMCT scanning of Pipe S. The numerical yield strength loci of the sublayers were calculated in (σ_{eq}^{VM}, σ_H)-space. The analytical yield function in Eq. 7 was fitted to each of the numerical yield loci, which produced unique sets of values for the two yield function parameters (σ_y and α) of each sublayer. Strong correlations were found between the model parameters and the average porosity f of the sublayers. The analytical expressions of Eq. 17 and Eq. 18 were fitted to the (σ_y, α) versus f data. The parameter values are given in Table 5 and the expressions are plotted in Fig. 7 – along with the expressions of the original implementation (i.e. Eq. 13 and Eq. 14). In Fig. 7(a), some differences is seen between the original expression and Eq. 18 of the modified model, where the latter is seen to saturate at large values of f. This may potentially present a source of deviation between the two relations at porosity values high above $f = 0.3$. However, the porosity of in coatings are not seen to increase significantly above this value for the applied load cases. Therefore, f will mostly be equal to or less than the initial assigned value (which is given in Section 5.1) for the simulations presented herein.

Table 5
Calibrated parameters for Eq. 13 and Eq. 14 of the original model, and Eq. 17 and Eq. 18 in the modified model, which are plotted in Fig. 7.

	B_1	B_2	C_1
Eq. 13	2.03	0.45	–
Eq. 14	–	–	2.46
Eq. 18	1.06	-15.14	–
Eq. 17	–	–	2.46

4.3. Fracture

The fracture criterion given in Section 3.5 uses a critical damage variable $\Psi_{critical}$, which governs element erosion. As with the strain-rate and temperature sensitivity of the polypropylene material found in the coatings, the experimental characterization of $\Psi_{critical}$ is considered to be outside the scope of this work. Therefore, the calibration of the fracture parameter is based on inverse modeling of a component test. A value of $\Psi_{critical} = 1.3$ was seen to produce good correspondence between the

preliminary simulations and the corresponding experimental results. This value is within reasonable bounds of the fracture strain presented in [21]. The limit porosity for damage accumulation f_{limit} in Eq. 20 was put equal to 1%.

5. Numerical modeling and simulations

5.1. Preliminary

This section presents the results from the simulations of the full-scale component tests outlined in Section 2.3 for Pipe S and Pipe L using the calibrated models for the X65 steel and the coating material introduced in Section 2.1 and Section 3, respectively. The coatings are discretized into sublayers (independent of the multi-layer design in Fig. 1) along r. The thickness of each sublayer region is approximately 2 mm for both designs. This yields a total of 24 and 40 sublayers for the coating sections of Pipe S and Pipe L, respectively. Fig. 8 presents the sublayer schemes using different colors for the individual sublayers imposed over the macroscopic pore morphology (retrieved by XRMCT) of both designs. The colors used on the cross-section of Pipe S corresponds to the marker colors of Fig. 7. Apart from strain-rate and temperature effects, the mechanical behavior of these sublayers is governed by the average porosity. The average porosities of the sublayers (used as the initial porosity in the simulations) are presented in Fig. 8. The porosities are calculated based on the voxel values in the XRMCT data confined by each sublayer. This approach of using the XRMCT data to estimate the porosity was validated against weight/volume measurements by Vestrum et al. [16]. The setup rendered in Fig. 2 is modeled in Abaqus/CAE and all simulations are run in Abaqus/Explicit (version 2017) with the coating models implemented via the VUMAT subroutine interface. The indenter geometry and lower support are modeled as discrete rigid and analytical rigid surfaces, respectively. A single mesh was used for each of the pipeline designs, i.e. remained constant across all analyses presented. The elements in the impact region (where the field variable

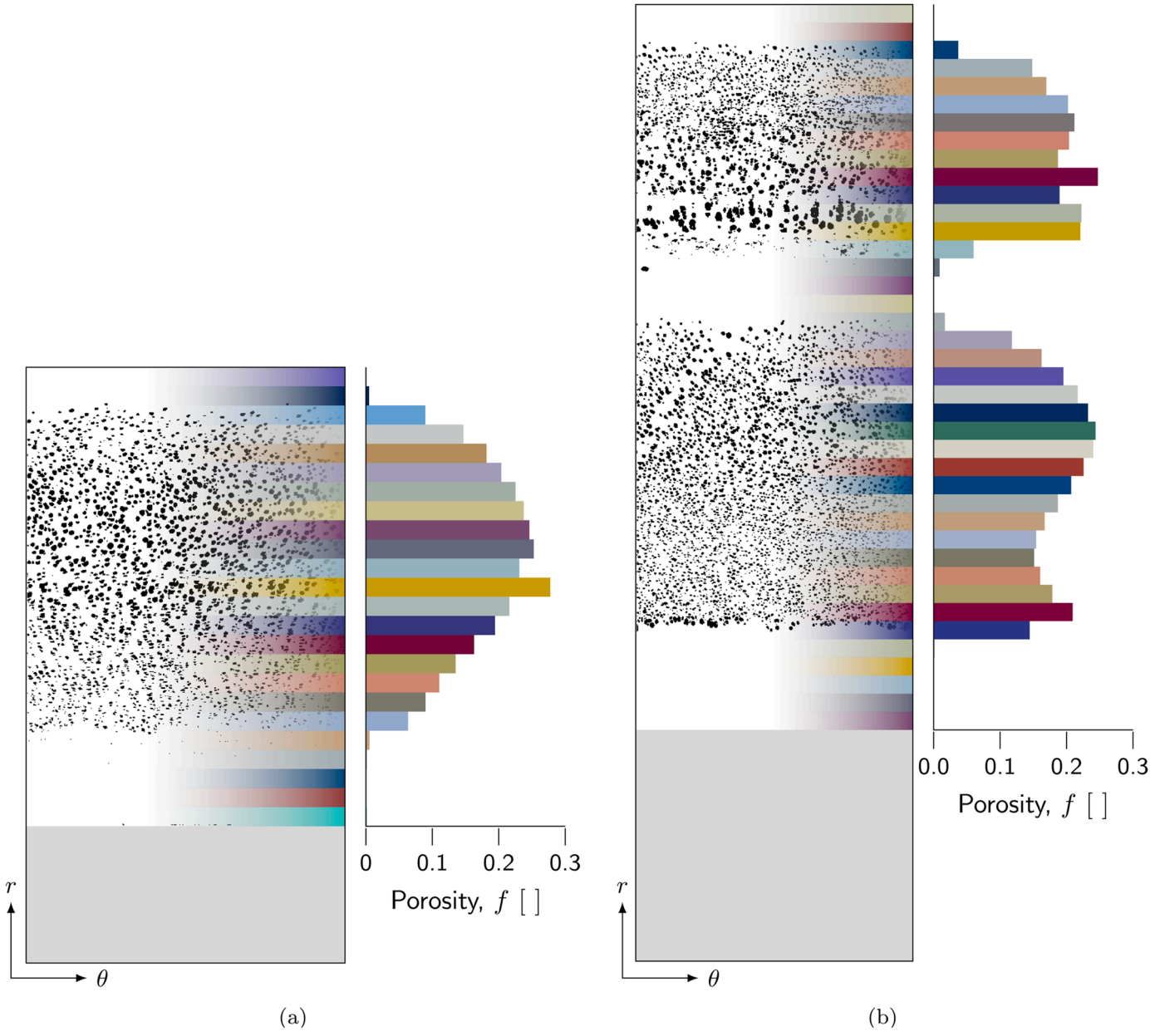

Fig. 8. Illustrations of the pore morphologies retrieved from XRMCT of (a) Pipe S and (b) Pipe L with the corresponding sublayer schemes overlaid. The initial average porosity f for each sublayer is also plotted on the right-hand side of each illustration.

gradients were large) were approximately 2 mm in all three directions while gradually increasing in size when moving away from this zone. Mesh sensitivity studies were performed during the development of the models in order to ensure convergence while at the same time keeping the computational time reasonable. All elements were of type C3D8R with enhanced hourglass and distortion control. Contact was modeled using the penalty formulation under general contact with an overall friction factor of 0.2, which was chosen based on the parametric studies conducted in the preliminary simulations. Due to the symmetry of the problem, only one half of the specimen was modeled with the symmetry plane defined by the $r - z$ directions.

Different model configurations and temperature conditions have been used in the simulations. The model configurations relate to whether various model features (i.e. fracture, strain-rate sensitivity and thermal softening) are enabled. An identification system using labels was employed where the modified model was identified with the letter M, fracture (F) states if element erosion was enabled, while strain-rate sensitivity (S) or thermal softening (T) indicate if the corresponding terms in Eq. 15 are enabled. Table 6 contains the labeling scheme used to differentiate between the model configurations.

Section 5.2 contains the simulations of the uncoated specimens, while Section 5.3 and Section 5.4 present simulations of the quasi-static indentation and impact tests without any viscous effects in the coating in Section 5.4. Section 5.5 presents a set of case studies where different model configurations of the modified model are used to simulate the impact tests under various temperature conditions.

5.2. Quasi-static indentation of uncoated specimens

Uncoated quasi-static indentation experiments (Table 3) are simulated in order to validate the constitutive model of the X65 steel. A hypoelastic-plastic formulation with nonlinear geometry effects, work-hardening according to the two-term Voce law presented in Section 2.1 and von Mises plasticity was applied to model the X65 steel sections of both Pipe S and Pipe L.

Fig. 9 and Fig. 10 present the force-deformation data during quasi-static indentation of uncoated Pipe S and uncoated Pipe L components, respectively. The deformation measurements are illustrated in Fig. 2, while the force measure F is the reaction force parallel to the loading direction. The tests ID stated in the parentheses in the figure labels correspond to that used by Vestrum et al. [15], which are declared in Table 3. In Fig. 9(b) and Fig. 10(b) it may be seen that the values for u_i stop at approximately 50 mm and 18 mm, respectively. This was due to the previously mentioned problems in the test setup where the device used for logging reached its maximum. While the simulation of Pipe S is seen to correspond better with the experiments than for Pipe L, the results are deemed to be generally comparable. At large deformations, the results are seen to diverge with differences of approximately 50 kN and 200 kN at the greatest comparable deformation points for Pipe S and Pipe L, respectively. These results were considered reasonable, so the presented constitutive model for the X65 steel was applied in the subsequent analyses.

5.3. Quasi-static indentation of coated specimens

The indentation response of coated specimens of Pipe S and Pipe L under quasi-static loading conditions was then analyzed. Time-scaling, equivalent to mass scaling in rate-insensitive models, was used in the simulations, and efforts were made to ensure that dynamic effects were neglectable [27]. As previously mentioned, it quickly became apparent during preliminary simulations that it was necessary to replicate the rupturing observed in the indentation region of the experiments. Model configuration M2 was introduced for this purpose.

Fig. 11 and Fig. 12 presents the results produced by quasi-static indentation simulations with the results from the experiments for Pipe S and Pipe L, respectively. Black markers have been added to the figures, which indicates where numerical issues (e.g. a significant drop in critical time step, contact issues or automatic termination of the analyses due to excessive element distortion) start to occur in the models when element erosion is disabled. The IDs in the legends correspond to the tests declared in Table 3. In Fig. 13, cross-section deformation with fringe plots showing porosity at different times during indentation of test QL2a (Fig. 12).

The simulations are seen to produce very good correspondence with the experiments in terms of force-deformation data when fracture is enabled. Element erosion is seen to induce small oscillations in the data, but the correct slope is maintained. The simulations are seen to reproduce the sudden rise in force-levels as the indenter engages the steel, with especially good correspondence for Pipe L. For Pipe S, a slight premature change is seen in Fig. 11(a). The exact cause of this is unknown, but it may be related to a mismatch between the actual and modeled coating thickness in the indentation zone. Good correspondence is seen in the initial deformation of the steel, but a slight overestimation is observed at large deformations.

5.4. Impact on coated specimens

The impact tests were simulated using coating model configuration M2. M2 includes none of the addition features of the modified model making it comparable to the original implementation, but with an inclusion of f in the return-mapping implementation (see Eq. 18). The same setup was used in the impact simulations as in the quasi-static

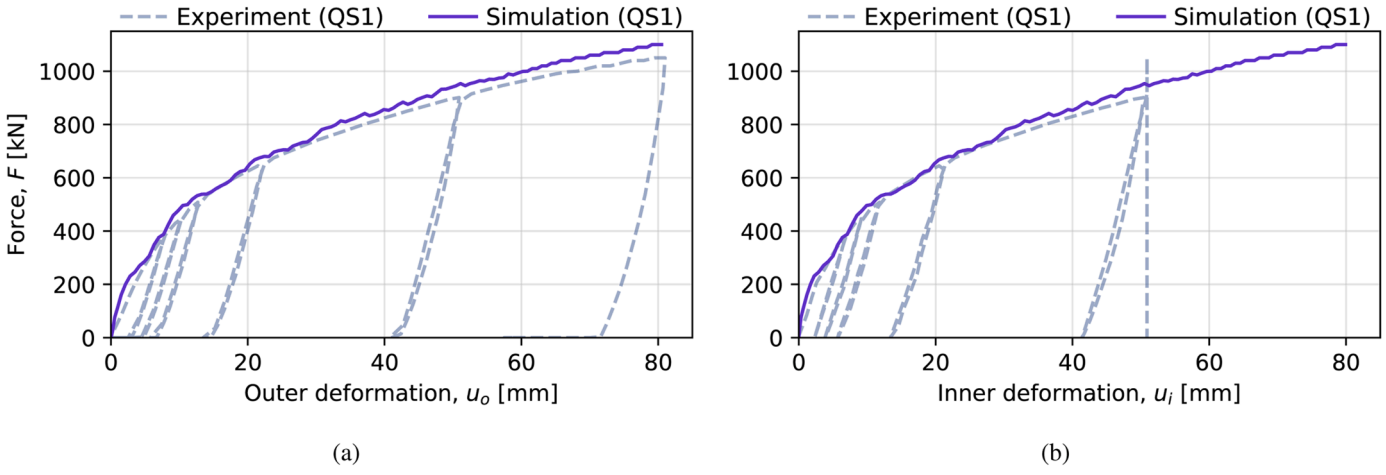

Fig. 9. Quasi-static indentation of an uncoated Pipe S specimen. The cut-off seen in the inner deformation values was related to a problem in the test setup.

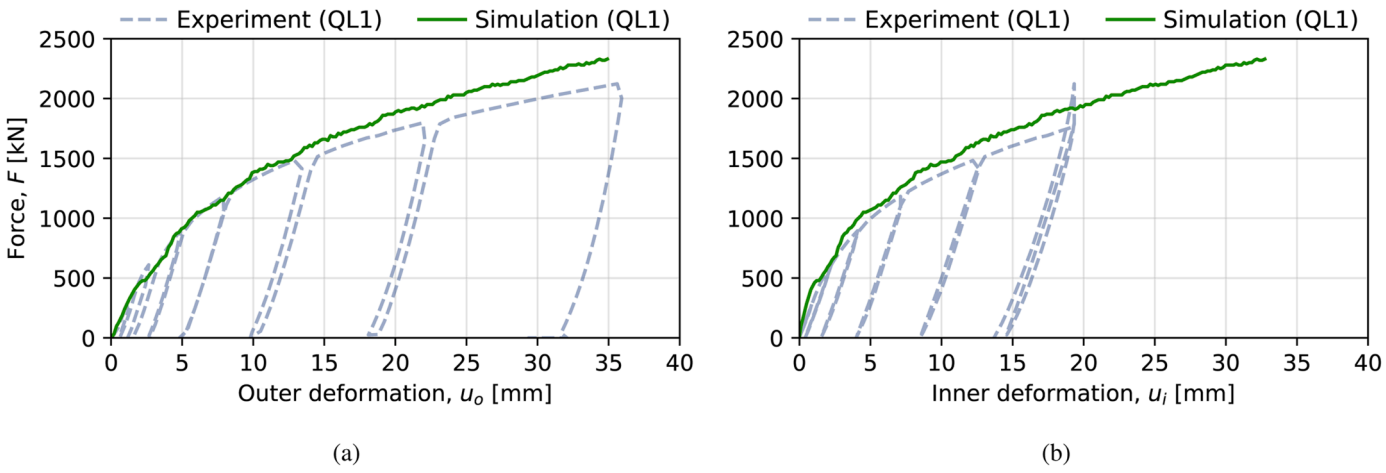

Fig. 10. Quasi-static indentation of an uncoated Pipe L specimen. The cut-off seen in the inner deformation values was related to a problem in the test setup.

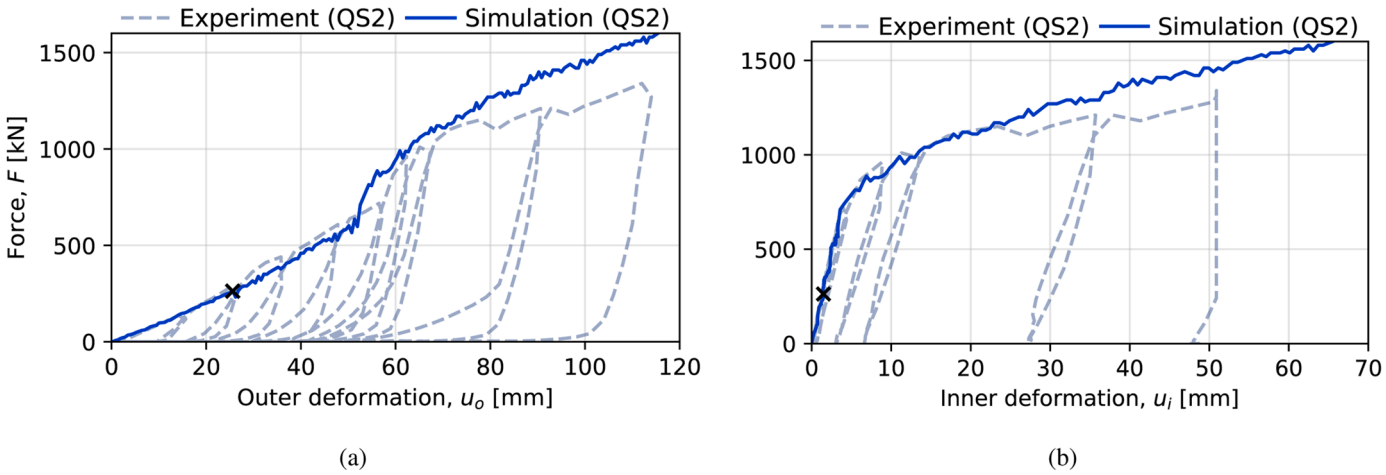

Fig. 11. Quasi-static indentation of a coated Pipe S specimen (test QS2). The markers indicate where numerical issues arise using the original constitutive model. The blue graph uses model configuration M1-F.

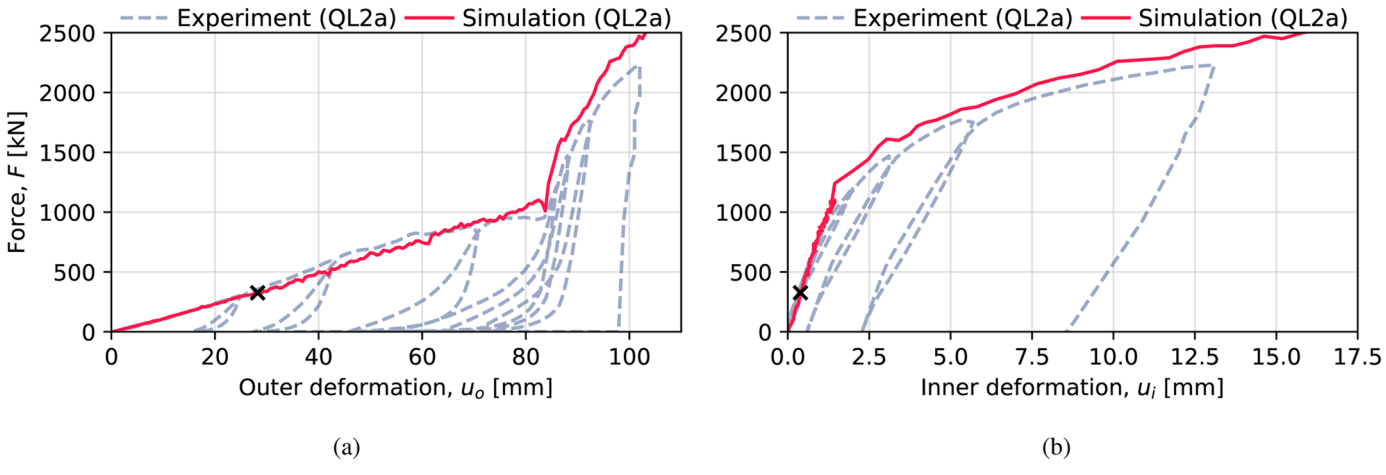

Fig. 12. Quasi-static indentation of a coated Pipe L specimen (test QL2a). The markers indicate where numerical issues arise using the original constitutive model. The red graph uses model configuration M1-F.

indentation simulations, but instead of displacing the indenter, an initial velocity was imposed to the indenter in accordance with Table 3. The mass of the indenter was equivalent to that indicated in Fig. 2. For these analyses, element erosion was disabled to facilitate the study of how the strain-rate and temperature sensitivity influences the global force-displacement results. This will be further investigated in Section 5.5.3.

Fig. 14 presents the results produced for simulations of DS4a, DL4a and DL2a with no fracture, temperature or strain-rate effects considered

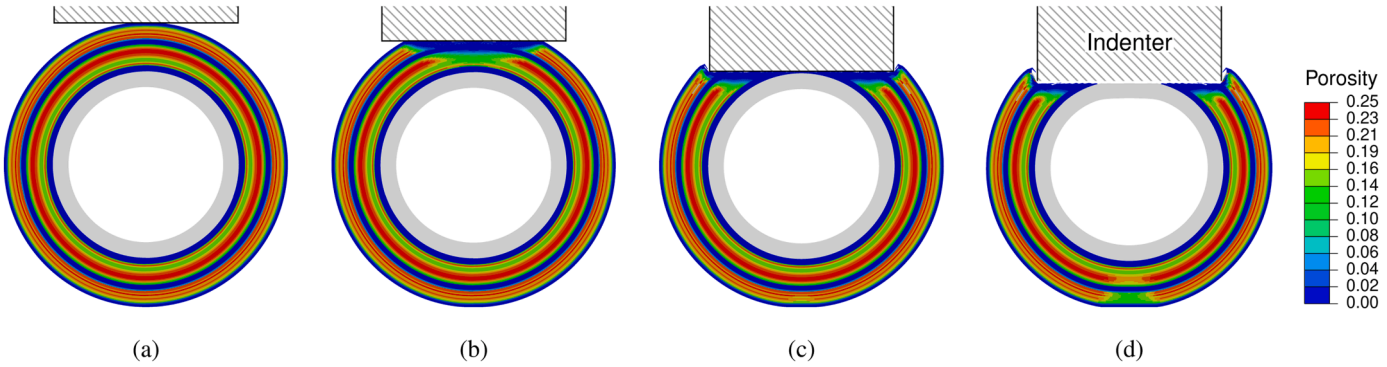

Fig. 13. The cross-section at the point of indentation during simulation of test QL2a for outer deformation values of (a) $u_o = 1$ mm, (b) $u_o = 31$ mm, (c) $u_o = 81$ mm and (d) $u_o = 100$ mm. The fringe plots are showing porosity.

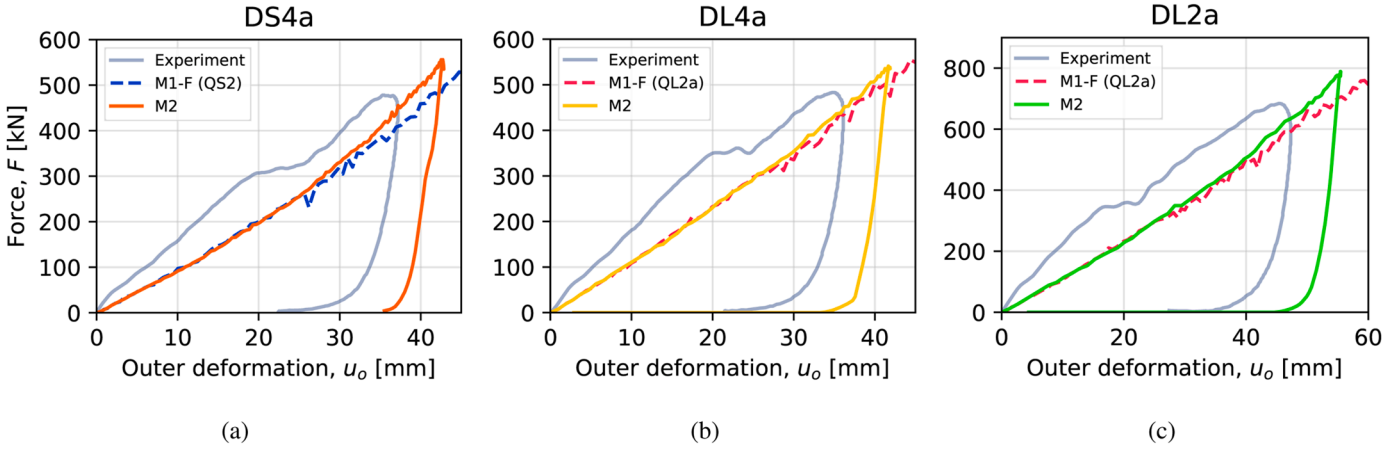

Fig. 14. Comparison between experiments and simulations of (a) DS4a, (b) DL4a and (c) DL2a. The legend labels correspond with the labeling scheme given in Table 6.

Table 6
Overview of labels used for the various configurations of the modified model used in the simulations in Section 5.

Label	Version	Fracture	Strain-rate	Temperature
M1-F	Modified	Yes	No	No
M2	Modified	No	No	No
M3-S	Modified	No	Yes	Yes
M4-FS	Modified	Yes	Yes	Yes
M5-ST	Modified	No	Yes	Yes

(i.e. model configuration M2), along with the results from the quasi-static simulations using M1-F. It is reminded that M1-F includes fracture, while M2 does not. This induces a difference in slope between the presented simulation results and the oscillations seen for M1-F. Otherwise, the comparativeness of the results comes as no surprise as time scaling was used for the quasi-static analyses where the quasi-static loading velocities applied were comparable to those achieved during the impact tests. As M2 does not consider any material viscous phenomena, the lack of inertial effects will produce comparable force levels between the quasi-static and dynamic simulations – up to the point where the kinetic energy of the indenter is dissipated and the forces drop rapidly. The slopes in the force response in all three tests are first underestimated in the simulations compared to the corresponding experiments. However, the slopes are seen to be more comparable during elastic rebound.

5.5. Case studies

5.5.1. Preliminary

This section presents the simulations of the impact tests using the modified coating model, which were performed to investigate how the implemented strain-rate and temperature sensitivity influences the simulation results. Different cases were studied using the model configurations presented in Table 6. The case studies include simulations of the impact tests using:

- Model configuration M3-S at constant coating temperature of T = 23°C (i.e. room temperature)
- Model configuration M4-FS at T = 23°C (i.e. room temperature)
- Model configuration M5-ST using temperature fields produced from steady-state thermal analyses

The first two cases (using M3-S and M4-FS) are thought to represent the actual conditions of the impact tests at room temperature. M4-FS is essentially equal to M3-S, but with fracture enabled. In the third case (M5-ST), temperature fields (one for each of the two pipeline designs) are used as input to the simulations in order to study how a temperature variation through the coating layer influence the global response of the pipeline during impact events. While not comparable to the actual temperature conditions of the component tests, this could potentially be an important aspect to consider as the fluid flow conveyed in the pipelines may reach relatively high temperatures compared to the temperatures of the ambient seawater, which may contribute to a graded mechanical behavior in the coating material. The procedure necessary in

producing the said temperature fields are presented in Section 5.5.2.

5.5.2. Temperature fields

XRMCT-based unit cell models for each of the sublayers were derived and used to estimate the thermal conductivity coefficients in the three principal directions defined in Fig. 1. The approach of estimating the thermal conductivity gradient is similar to the one by Hegdal et al. [31], who employed digital images of microtome slices taken of a similar coating product to derive finite element models. The conductivity coefficients were used as input to the material definition of the corresponding sublayer. Following this, the steady-state (i.e., constant in time) temperature fields for both pipeline designs were produced using a fictitious, but realistic, temperature scenario. This scenario was represented by applying temperature boundary conditions of 100°C and 4°C to the inner surface of the pipeline steel hull and the outer surface of the coating, respectively. The former boundary condition reflects the temperature of the fluid flow and the latter represents the temperature of the ambient seawater. The resulting temperature fields were then imposed on the component geometries and used in the simulations of the dynamic impact component tests using M5-ST.

In order to produce these fields, it was first necessary to estimate the thermal properties of the sublayers across the coating thickness. The two-phase design of the porous solid produces a complex thermal conduction interaction, which is the combined outcome of the macroscopic morphology and the individual thermal properties of the constituents in the two phases. Analogue to the approach taken by Vestrum et al. [17], where the mechanical behavior of each sublayer was studied, the XRMCT-based models of the sublayers were used to study the thermal conduction across the coating. The post-processing procedure illustrated in Fig. 5 was utilized to derived hexagonal element meshes of the porous structure as illustrated in Fig. 15(a). In [17], the pores were modeled as empty voids to reduce the computational demand of the explicit analyses. However, as steady-state thermal simulations are implicit analyses and consequently less resource demanding, the pore phase was meshed and given material properties corresponding to CO_2 gas. This modeling is illustrated in two dimensions in Fig. 15(b) where the pores are given the properties of CO_2 represented by a beige color. The simulations only consider thermal conduction, while heat transfer by convection or radiation is neglected. Herein, each sublayer unit cell model had dimensions 2 mm × 16 mm × 16 mm, and a three-dimensional example of an XRMCT-based model is given in Fig. 16(a) where the two macroscopic phases are illustrated. An arbitrary temperature difference of $\Delta T = 20$ K was imposed by placing temperature boundary conditions on each of the two opposing model faces with surface normals parallel to the respective direction. The thermal conductivity coefficients of the solid and gaseous phases were put to $k_{PP} = 0.22$ W/mK and $k_{CO_2} = 0.015$ W/mK, respectively. The simulations were steady-state and done in Abaqus/Standard (version 2017). Fig. 16(b) illustrates the flow of heat energy (i.e., the heat flux) in the r-direction for the same sublayer model as in Fig. 16(a) from one of the thermal analyses. When comparing the model in Fig. 16(a) and the color contours of Fig. 16(b), it is readily seen that the thermal conductivity is lower in the pore phase than in the solid phase across the sublayer.

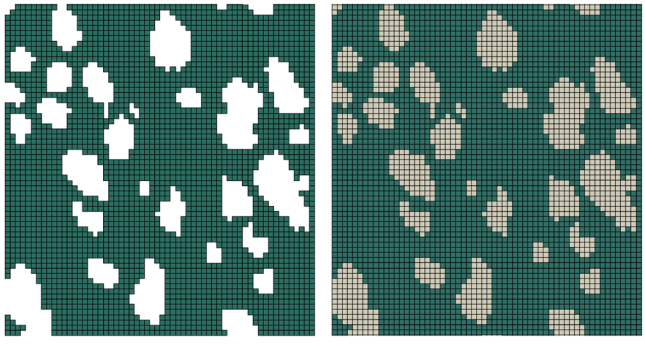

(a) (b)

Fig. 15. FE models (a) excluding and (b) including discretization of the pore phase for the cross-section slices from Figure 5.

Steady-state thermal conduction for an isotropic medium is modeled by Fourier's law where the flow rate of heat energy per unit area through a surface is linearly proportional to the negative temperature gradient. The one-dimensional formulation of this law in direction i may be written as

$$q_i = -k_i \frac{dT}{di} \quad \Rightarrow \quad k_i = -\frac{q_i}{dT/di} \quad \text{for} \quad i = \{r,\ \theta,\ z\} \tag{24}$$

where q_i is the heat flux density, k_i is the thermal conductivity coefficient and dT/di is the temperature gradient. A total of 72 thermal simulations were run for Pipe S (24 sublayer models × 3 directions) and 120 simulations for Pipe L (40 sublayer models × 3 directions). Fig. 17 and Fig. 18 present the thermal conduction coefficients for the three principal directions normalized with k_{PP} as a function of the normalized r-dimension denoted $\bar{r}$ for Pipe S and Pipe L, respectively. A distinct variation in the thermal conductivity is seen through the thickness of both coatings and there are also some noticeable deviations between the three principle directions. Nevertheless, as the steady-state solution of the outlined thermal scenario is of interest for our case, only the thermal conductivity coefficients along r (Fig. 17(a) and Fig. 18(a)) are used for establishing the temperature fields.

Full-scale steady-state thermal simulations were run using the same FE meshes as in the mechanical simulations. The conductivity coefficients were used as input to the material definition of the corresponding sublayer in the coating along with a thermal conductivity coefficient of 55 W/mK for the X65 steel. The steady-state temperature fields for both pipeline designs were produced using the fictitious temperature scenario described above. The resulting temperature fields were then imposed on the component geometries and applied in the simulations of the dynamic impact component tests using M5-ST. Fig. 19 presents cross-sectional contour plots of the temperature fields produced with the prescribed boundary conditions and the thermal conductivity coefficients from Fig. 17(a) and Fig. 18(a) for Pipe S and Pipe L, respectively. These temperature fields are used as input for the modified coating model.

A validation study was conducted to investigate the validity of the thermal properties produced in the previous section. An overall thermal conductivity between 0.165 and 0.185 W/mK is stated in the coating solution's data sheet [20]. A full through-thickness XRMCT-based coating model of Pipe S was produced and the thermal conductivity was estimated as a check. The model geometry had dimensions 48 mm × 4 mm × 4 mm with just under 1.4 million elements. Using the same estimation approach as for the sublayer models, the through-thickness thermal conductivity coefficient was estimated to 0.173 W/mK, which is well within the range supplied by the producer [20]. Thus, the approach is considered reasonable.

5.5.3. Dynamic impact using the modified constitutive model

Fig. 20 presents the results from the dynamic impact simulations for DS4a, DL4a and DL2a under various conditions using different coating model configurations. The previously presented data from M2 is restated to better evaluate the importance of modeling viscous and thermal material effects. Obvious trends are shared between the evaluated component tests. A clear effect of including dependence of the strain rate in the coating response is seen on the force levels produced by the impact simulations at room temperature (M3-S). The increased slopes in the force-outer deformation measures are seen to produce results more comparable with the experiments. It is noted that the applied fracture criterion does not make a significant difference to the results (M4-FS) in these simulations. While the peak force is somewhat overestimated in all

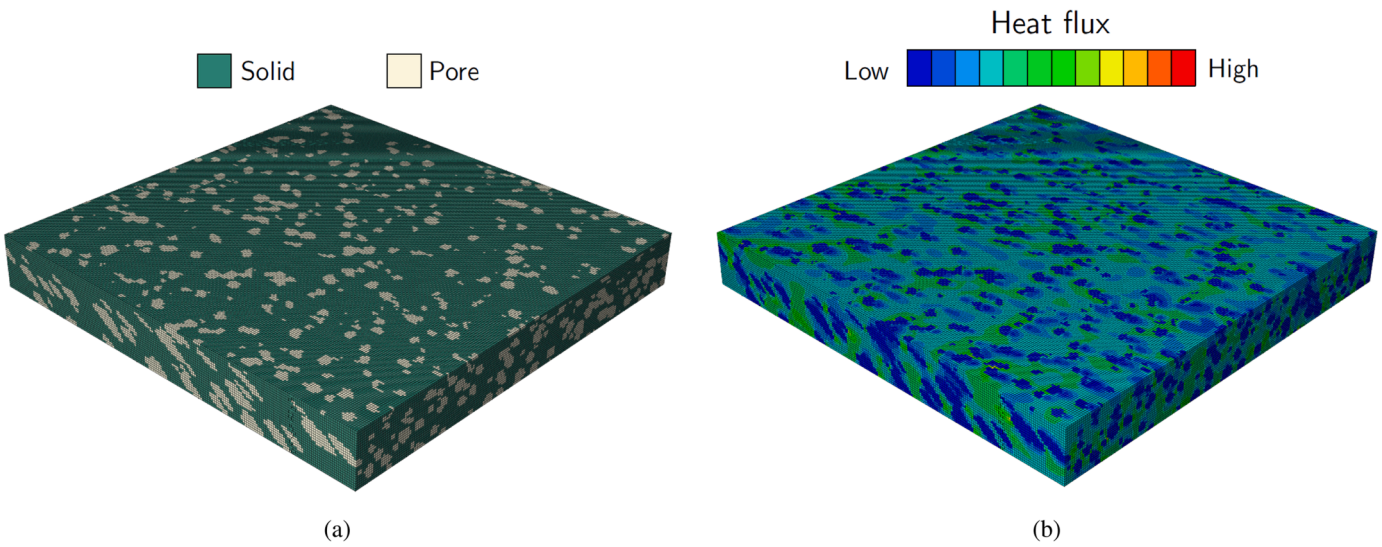

Fig. 16. (a) One of the bin models and (b) a contour plot of the heat flux in r-direction.

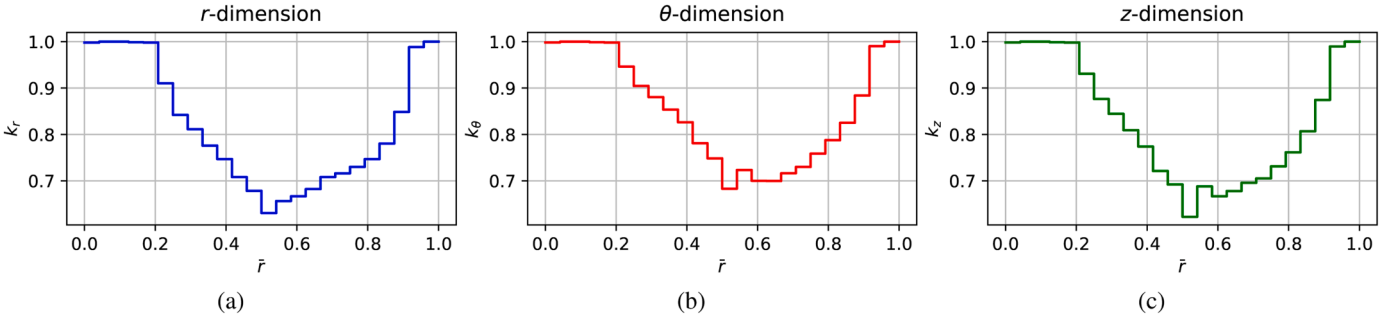

Fig. 17. Normalized heat conductivity coefficient as a function of Pipe S coating thickness in the (a) r-, (b) θ- and (c) z-direction.

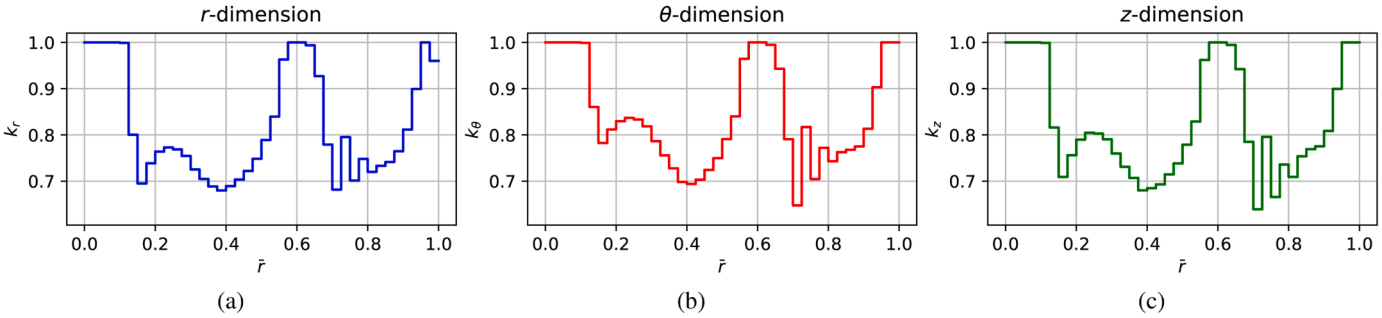

Fig. 18. Normalized heat conductivity coefficient as a function of Pipe L coating thickness in the (a) r-, (b) θ- and (c) z-direction.

analyses presented in Fig. 20, the final outer deformation is seen to be similar to that of the corresponding experiment. The given temperature scenario is also observed to lower the slope at extended deformations and the final peak force (M5-ST).

6. Discussion

It was seen that the original coating model reproduced the initial response of the quasi-static experiments well. However, it became apparent that it was necessary to delete elements in the ligament between the indenter and the steel pipe in order to have reliable results. The major points taken from the work related to the simulation of the quasi-static indentation experiments are outlined and discussed sequentially below:

- When a rigid indenter is forced into the softer coating, the cross-sectional deformation is initially confined to the intermediate region. Since the coating strength decrease with increasing porosity, the deformation localizes in the most porous regions. As the indenter is displaced farther into the coating, the porous material becomes compressed and densifies. This effect is captured by the porosity evolution in the coating model. The deformation of the inner steel pipe remain small up to this point and the correspondence between the constitutive model and experiments is very good in general.
- Significant deviations between the numerical and the experimental results (in addition to numerical problems) arise if the indenter is further displaced into the coating after this point. Rupturing in the coating ligament between the indenter and the steel pipe was evident in the experiments. The rupturing of the coating contributed to a

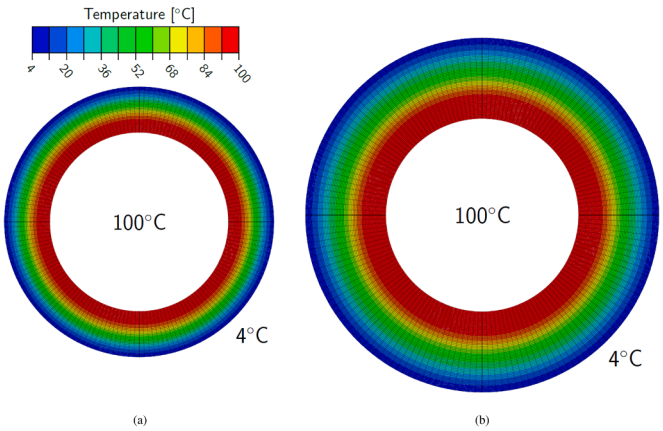

Fig. 19. Temperature distribution with $T_{\text{inner}} = 100°C$ and $T_{\text{outer}} = 4°C$ across cross-sections (a) Pipe S and (b) Pipe L.

decrease in the slope of the force-outer deformation data. However, the original coating model had no fracture modeling included. This leads to overcompression of the coating and numerical problems. A simple strain- and porosity-based fracture criterion was implemented to alleviate this issue, which proved to be very effective. The mentioned numerical problems almost completely remedied allowing the simulations to run more efficiently as the critical time step maintained at a reasonable level and the correspondence in force-displacement data was improved.

The modified coating model was seen to perform well. The main observations from the simulations using the modified coating model were:

- While Vestrum et al. [15] concluded that the results from the quasi-static indentation experiments could be used to estimate the full-scale component response under impact loading, some elevated force levels are seen in the impact experiments. The strain-rate sensitivity of the modified model is seen to improve the predicted response by elevating the forces. Good correspondence with the dynamic tests is produced, but it is reminded that the material data used to calibrate the model does not necessarily represent the exact strain-rate and temperature sensitivity of the actual polymer material found in the coating. While a similar characterization should be performed for the respective material in the future, this is beyond the scope of this work. Nevertheless, the effect of including strain-rate dependence in the coating is obvious.
- The same impact experiments were analyzed with a fictitious (but realistic) temperature scenario. The significant gradients in the resulting temperature fields induce yet another contribution to the graded nature of the coating material's yield strength, which may be expected while the pipeline is in operation. A slight change of the slope at the last stages of deformation is seen, which reduces the peak force slightly. From Fig. 19, it is readily seen that significant portions of both coatings are exposed to temperatures above 23°C (i.e. above room temperature), which induces a relative lowering of the yield strength. It is difficult to assess the combined effect that the temperature and porosity gradients, but the deformations are observed to be more spread out across larger coating sections using the imposed temperature fields than at room temperature.

The thermal study presented in this work poses another possibility not yet mentioned. In the aftermath of an impact event, it is important that the coating still retains its function as a thermal insulator. It is shown that it is possible to run full-scale thermal simulations by deriving a model that associates the thermal properties of an undamaged coating to its pore morphology. While this work has demonstrated the capabilities provided by the constitutive coating model in estimating the structural integrity of coated pipelines, it is argued that the model also presents a means of evaluating the thermal properties of the cross-section after impact events. Although out of scope for this work, it may be possible to assess the insulation effectiveness of a damaged pipeline by evaluating the porosity distribution of its coating or to optimize the insulation ability by changing/modifying the macroscopic pore morphology.

7. Concluding remarks

This work has investigated the performance of the constitutive model proposed by Vestrum et al. [17] for porous polymer pipeline coatings by simulating the mechanical response of pipelines during quasi-static indentation and impact tests. Modifications have been proposed to the model in order to include temperature and strain-rate effects, and the importance of these effects has been evaluated. The modified model was calibrated based on material data found in the literature and the material effects were studied. A strain- and porosity-based fracture criterion was also included. In addition, the thermal conductivity of the coating was mapped in the three principal directions of the pipeline for each sublayer, and a realistic temperature scenario was used to simulate numerical temperature fields. The temperature fields were used with the

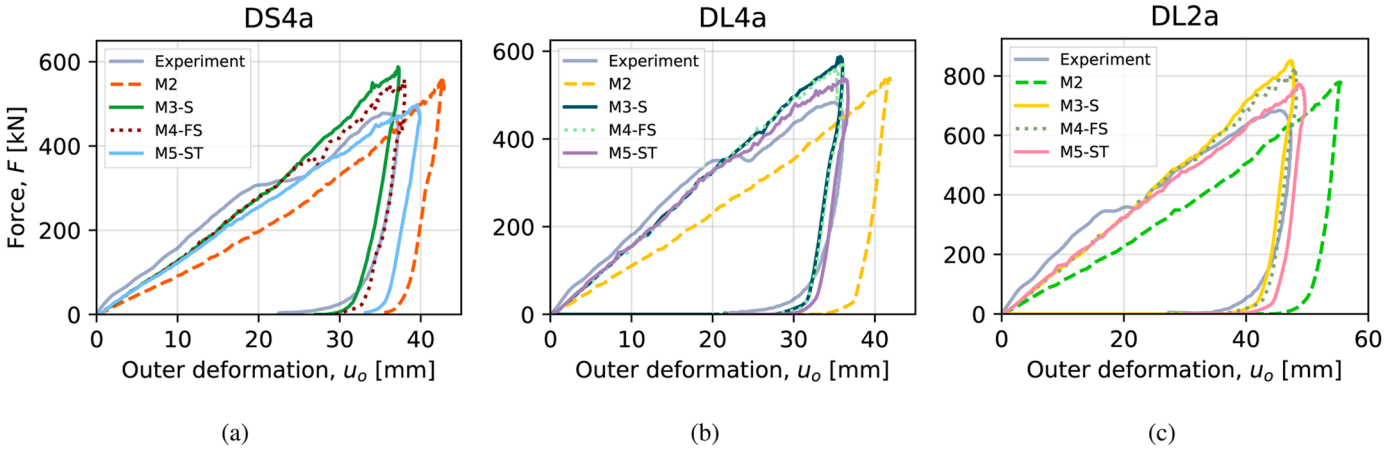

Fig. 20. Comparison between experiments and simulations of (a) DS4a, (b) DL4a and (c) DL2a with the modified coating model. The legend labels correspond with the labeling scheme given in Table 6.

modified model to investigate the influence of temperature gradients on the pipeline components' global response during impact loading. The following main conclusions are made about the constitutive coating model:

- The constitutive modeling approach applied to the coating material is seen to accurately reproduce the force-displacement response during quasi-static indentation when fracture modeling is included. The porosity evolution of the model is seen to introduce a strengthening in regions where the deformation initially localized, thus keeping the regions from becoming excessively deformed up until the point where the coating is fully densified. A precise correspondence was achieved well into yielding of the inner steel pipe, but there was a slight overestimation in the simulations at extended indentation for both pipeline designs.
- The XRMCT-based modeling approach is seen to provide a good tool for estimating the thermal properties of the graded porous polymer, which allows for simulating the temperature fields in components during given temperature scenarios. It is also argued that this approach may be used to estimate the thermal properties of insulating coatings succeeding impact events.
- With no strain-rate effects included, the force-displacement behavior was underestimated in comparison with the experiments. The force levels produced by including strain-rate effects were seen to approach the experimental results, but still with some deviations. It is believed that the modified formulation proposed represents the phenomena in a good manner, but that proper characterization of the viscous, thermal and fracture response of the constituent material is suggested for further work.

The work presented herein serves as an effective modeling framework for analyzing the behavior of porous polymer coated pipelines under various load cases. It is argued that the impact scenarios studied in this work induces a complex situation in the vicinity of the impact region where several material phenomena must be represented. The coating model is shown to be a highly versatile framework where such material phenomena can be accounted for with minor efforts to produce reasonable results. To this end, it is concluded that the proposed modeling approach serves as a valuable technique for assessing future pipeline designs.

CRediT authorship contribution statement

Ole Vestrum: Conceptualization, Methodology, Software, Formal analysis, Validation, Writing - original draft, Writing - review & editing. **Magnus Langseth:** Supervision, Writing - original draft, Writing - review & editing, Funding acquisition. **Tore Børvik:** Conceptualization, Supervision, Writing - original draft, Writing - review & editing, Funding acquisition.

Declaration of Competing Interest

The authors declare that they have no known competing financial interests or personal relationships that could have appeared to influence the work reported in this paper.

Acknowledgments

The present work has been carried out with the financial support from Centre for Advanced Structural Analysis (CASA) through the Research Council of Norway's Centre for Research-based Innovation (SFI) scheme (project 237885). The authors also gratefully acknowledge Equinor for supplying the pipeline coating samples.

References

[1] Brown R. OTC 1570 Pipelines can be designed to resist impact from dragging anchors and fishing boards. Offshore Technology conference 1972. https://doi.org/10.4043/1570-MS.
[2] DNV GL. DNVGL-RP-F111 Interference between trawl gear and pipelines2017; Recommended practice.
[3] de Groot S. The impact of laying and maintenance of offshore pipelines on the marine environment and the north sea fisheries. Ocean Management 1982;8(1):1–27. https://doi.org/10.1016/0302-184X(82)90011-7.
[4] Igland R, Søreide T. OMAE2008-57354 Advanced pipeline trawl gear impact design. International Conference on Offshore Mechanics and Arctic Engineering 2008;3: Pipeline and Riser Technology; Ocean Space Utilization:271–7. https://doi.org/10.1115/OMAE2008-57354.
[5] Howell GR, Cheng YF. Characterization of high performance composite coating for the northern pipeline application. Progress in Organic Coatings 2007;60(2):148–52. https://doi.org/10.1016/j.porgcoat.2007.07.013.
[6] The Petroleum Safety Authority Norway. Rørledningsskader - Skader og hendelser fra Petroleumstilsynets CODAM database. https://www.ptil.no/contentassets/a13ec8ed3fc94e3a97b76aebb01bf6e3/roerledningsskader-2018-okt.pdf; 2018. [Online; accessed 1-December-2019].
[7] Gjertveit E, Berge J, Søvik B. OTC 20814 The Kvitebjørn Pipeline Repair. Offshore Technology Conference 2010. https://doi.org/10.4043/20814-MS.
[8] Soares C, Søreide T. Plastic analysis of laterally loaded circular tubes. Journal of Structural Engineering 1983;109(2). https://doi.org/10.1061/(ASCE)0733-9445(1983)109:2(451).
[9] Shen W, Chen K. An investigation on the impact performance of pipelines. International Journal of Crashworthiness 1998;3(2):191–210. https://doi.org/10.1533/cras.1998.0070.
[10] Palmer A, Touhey M, Holder S, Anderson M, Booth S. Full-scale impact tests on pipelines. International Journal of Impact Engineering 2006;32(8):1267–83. https://doi.org/10.1016/j.ijimpeng.2004.09.003.
[11] Manes A, Porcaro R, Ilstad H, Levold E, Langseth M, Børvik T. The behaviour of an offshore steel pipeline material subjected to bending and stretching. Ships and Offshore Structures 2012;7(4):371–87. https://doi.org/10.1080/17445302.2011.606699.
[12] Kristoffersen M, Casadei F, Børvik T, Langseth M, Hopperstad O. Impact against empty and water-filled X65 steel pipes - Experiments and simulations. International Journal of Impact Engineering 2014;71(Supplement C):73–88. https://doi.org/10.1016/j.ijimpeng.2014.04.004.
[13] Longva V, Sævik S, Levold E, Ilstad H. Dynamic simulation of subsea pipeline and trawl board pull-over interaction. Marine Structures 2013;34(Supplement C):156–84. https://doi.org/10.1016/j.marstruc.2013.09.004.
[14] Moshagen H, Kjeldsen S. OTC 3782 Fishing gear loads and effects on submarine pipelines. Offshore Technology Conference 1980. https://doi.org/10.4043/3782-MS.
[15] Vestrum O, Kristoffersen M, Polanco-Loria MA, Ilstad H, Langseth M, Børvik T. Quasi-static and dynamic indentation of offshore pipelines with and without multi-layer polymeric coating. Marine Structures 2018;62:60–76. https://doi.org/10.1016/j.marstruc.2018.08.001.
[16] Vestrum O, Langseth M, Børvik T. Finite element modeling of porous polymer pipeline coating using x-ray micro computed tomography. Composites Part B: Engineering 2019;172:406–15. https://doi.org/10.1016/j.compositesb.2019.04.028.
[17] Vestrum O, Dæhli LEB, Hopperstad OS, Børvik T. Constitutive modeling of a graded porous polymer based on x-ray computed tomography. Materials & Design 2020;188:108449. https://doi.org/10.1016/j.matdes.2019.108449.
[18] Kristoffersen M, Børvik T, Westermann I, Langseth M, Hopperstad O. Impact against X65 steel pipes - An experimental investigation. International Journal of Solids and Structures 2013;50(20):3430–45. https://doi.org/10.1016/j.ijsolstr.2013.06.013.
[19] Kristoffersen M, Børvik T, Langseth M, Hopperstad O. Dynamic versus quasi-static loading of X65 offshore steel pipes. The European Physical Journal Special Topics 2016;225(2):325–34. https://doi.org/10.1140/epjst/e2016-02629-4.
[20] Shawcor. Thermotite (Polypropylene foam). Shawcor; 2019Retrieved november 2019, Retrieved from https://cdn.shawcor.com/shawcor/files/85/85760b24-063d-484f-8f51-eaec69668329.pdf.
[21] Johnsen J, Grytten F, Hopperstad O, Clausen A. Influence of strain rate and temperature on the mechanical behaviour of rubber-modified polypropylene and cross-linked polyethylene. Mechanics of Materials 2017;114:40–56. https://doi.org/10.1016/j.mechmat.2017.07.003.
[22] Hanssen A, Auestad T, Tryland T, Langseth M. The kicking machine: A device for impact testing of structural components. International Journal of Crashworthiness 2003;8(4):385–92. https://doi.org/10.1533/ijcr.2003.0246.
[23] Tomasi C, Manduchi R. Bilateral Filtering for Gray and Color Images. Proceedings of the 1998 IEEE International Conference on Computer Vision 1998:839–46. https://doi.org/10.1109/ICCV.1998.710815.
[24] Otsu N. A Threshold Selection Method from Gray-Level Histograms. IEEE Transactions on Systems, Man, and Cybernetics 1979.
[25] Gibson L, Ashby M. Cellular Solids: Structure and Properties. Cambridge Solid State Science Series. 2. Cambridge University Press; 1997. https://doi.org/10.1017/CBO9781139878326.
[26] Deshpande V, Fleck N. Isotropic constitutive models for metallic foams. Journal of the Mechanics and Physics of Solids 2000;48(6):1253–83. https://doi.org/10.1016/S0022-5096(99)00082-4.

[27] Belytschko T, Liu W, Moran B, Elkhodary K. Nonlinear Finite Elements for Continua and Structures. 2. John Wiley & Sons, Ltd; 2013.
[28] Camacho G, Ortiz M. Adaptive lagrangian modelling of ballistic penetration of metallic targets. Computer Methods in Applied Mechanics and Engineering 1997; 142(3):269–301. https://doi.org/10.1016/S0045-7825(96)01134-6.
[29] Børvik T, Hopperstad O, Berstad T, Langseth M. A computational model of viscoplasticity and ductile damage for impact and penetration. European Journal of Mechanics - A/Solids 2001;20(5):685–712.
[30] Johnson G, Cook W. A constitutive model and data for metals subjected to large strains, high strain rates and high temperatures. Proceedings of Seventh International Symposium on Ballistic 1983.
[31] Hegdal JP, Tofteberg TR, Schjelderup T, Hinrichsen EL, Grytten F, Echtermeyer A. Thermal conductivity of anisotropic, inhomogeneous high-density foam calculated from three-dimensional reconstruction of microtome images. Journal of Applied Polymer Science 2013;130(2):1020–8. https://doi.org/10.1002/app.39238.